

# Tuning the Hydrophilic–Hydrophobic Balance of Molecular Polymer Bottlebrushes Enhances their Tumor Homing Properties

Parathan Ramamurthi, Zhongchao Zhao, Eamonn Burke, Nicole F. Steinmetz,\* and Markus Müllner\*

Nanoparticle (NP)-based drug delivery systems are promising in anticancer therapy, capable of delivering cargo with superior selectivity and achieving enhanced tumor accumulation compared to small-molecule therapeutics. As more efforts are being devoted to NP development, molecular polymer bottlebrushes (MPBs) have gained attention as a potential drug delivery vehicle. To date, the influence of various MPB parameters such as size, shape, and surface charge in determining tumor penetrability have been systematically probed. However, the role of amphiphilicity, specifically the hydrophilic–hydrophobic balance, remains unexplored. In this study, a series of MPBs are employed with varied hydrophobicity levels to reveal a dependence between MPB composition, cell association, and tumor homing. The data indicates that increasing levels of hydrophobicity in MPBs (to a certain level) demonstrate only marginal effects *in vitro* but reveals enhanced tumor homing in a mouse model of ovarian cancer *in vivo*, where more hydrophilic MPBs exhibit low tissue deposition and low tumor homing. In contrast, more hydrophobic MPBs show significant tumor accumulation and homing due to their engineered hydrophobicity.

## 1. Introduction

The concept of drug delivery to tumors aided by engineered nanoparticles (NPs) remains an active research area in nanomedicine. The motivation in using NPs for drug delivery derives from the added benefits they confer on the *in vivo* performance of their encapsulated drug load, including increased solubility and circulation times, protection from premature degradation and clearance, controlled drug release profiles and improved bioavailability.<sup>[1]</sup> Many of these benefits can be ascribed to the plethora of NP synthetic and functionalization techniques now available, which has led to a multitude of NP designs being reported as potential tumor-infiltrating agents.<sup>[2]</sup> While the development pipeline continues to grow, nanoparticles must be carefully engineered to overcome the various biological barriers to reach their target site *in vivo*.<sup>[3]</sup>

For example, for tumor homing applications, a remodeled extracellular matrix, heterogenous cell populations, oxygen and pH

P. Ramamurthi, E. Burke, M. Müllner  
Key Centre for Polymers and Colloids  
School of Chemistry  
The University of Sydney  
Sydney, NSW 2006, Australia  
E-mail: markus.muellner@sydney.edu.au

Z. Zhao, N. F. Steinmetz  
Department of NanoEngineering  
University of California, San Diego  
9500 Gilman Dr., La Jolla, CA 92039, USA  
E-mail: nsteinmetz@ucsd.edu

Z. Zhao, N. F. Steinmetz  
Center for Nano-ImmunoEngineering  
University of California, San Diego  
9500 Gilman Dr., La Jolla, CA 92039, USA

N. F. Steinmetz  
Department of Bioengineering  
University of California, San Diego  
9500 Gilman Dr., La Jolla, CA 92039, USA

N. F. Steinmetz  
Department of Radiology  
University of California, San Diego  
9500 Gilman Dr., La Jolla, CA 92039, USA

N. F. Steinmetz  
Moores Cancer Center  
Institute for Materials Discovery and Design  
University of California, San Diego  
9500 Gilman Dr., La Jolla, CA 92039, USA

M. Müllner  
The University of Sydney Nano Institute (Sydney Nano)  
The University of Sydney  
Sydney, NSW 2006, Australia

 The ORCID identification number(s) for the author(s) of this article can be found under <https://doi.org/10.1002/adhm.202200163>

© 2022 The Authors. Advanced Healthcare Materials published by Wiley-VCH GmbH. This is an open access article under the terms of the Creative Commons Attribution-NonCommercial License, which permits use, distribution and reproduction in any medium, provided the original work is properly cited and is not used for commercial purposes.

DOI: 10.1002/adhm.202200163

gradients and high interstitial fluid pressure can hinder access of these NPs into the tumor tissue. Indeed data indicate marginal improvements of tumor penetration levels of many NPs compared to free small molecules.<sup>[4]</sup> In response to these challenges, there has been a growing awareness within the nanomedicine field of the contributions of certain NP physicochemical properties on their transport and accumulation within tumors and biological systems. Hence optimization of physicochemical parameters of NPs is paramount to achieve sufficient accumulation levels and depth and deliver a therapeutically effective dose. Several key parameters such as size,<sup>[5]</sup> aspect ratio,<sup>[6]</sup> surface charge/chemistry,<sup>[7]</sup> and stiffness<sup>[8]</sup> have all been implicated in dictating the biodistribution patterns of nanomaterials, their cellular interactions and their ease of tumor penetration. By contrast, amphiphilicity (or the hydrophobic-hydrophilic balance) has been largely unexplored as a driver of NP behavior in biological environments. Data indicates that an amphiphilic character can exert a significant effect on a NP biodistribution and cellular uptake. For instance, studies employing copolymer NPs with different hydrophobicity could be derived from varying the ratio of N-iso-propyl acrylamide and N-*tert*-butyl acrylamide. The more hydrophobic particles were found to experience increased adsorption of the serum protein albumin onto their surfaces.<sup>[9]</sup> This finding was corroborated by Bewersdorff et al., who likewise observed that protein adsorption on amphiphilic polymer-based nanogels increased with increasing surface hydrophobicity. Follow-up *in vitro* experiments subsequently detected a rise in cell uptake of the more hydrophobic nanogels, which could be attributed to the formation of a larger protein corona.<sup>[10]</sup> Apart from modulating protein corona formation, amphiphilicity has been implicated in regulating NP-immune system interactions, wherein a positive trend between NP hydrophobicity and the strength of the consequent immune response was noted *in vitro* and *in vivo*.<sup>[11]</sup> Using computer-modelled NPs with hydrophobic and semi-hydrophilic profiles, Gu et al. simulated and investigated their interactions with lipid bilayer *in silico*, revealing key differences in the deformation patterns on the membrane depending on amphiphilicity.<sup>[12]</sup> Molecular dynamic simulations also revealed that varying the ratio of NP surface hydrophobicity to hydrophilicity affects the permeation behavior of NPs through membranes.<sup>[13]</sup> However, few studies that have methodically examined how tumor penetration and accumulation by NPs can be mediated by tuning their amphiphilicity via the hydrophilic–hydrophobic balance.

In that context, polymeric NPs based on molecular polymer bottlebrushes (MPBs) offer a synthetic platform that allow for customizing physicochemical parameters independently, and owing their modular synthesis and functionalization, they have been attracting increased attention as future drug-delivery carriers.<sup>[14]</sup> This branched macromolecule is produced from a single polymeric “backbone” densely grafted with numerous polymer “sidechains.” Because of the close proximity of sidechains, the backbone is forced out of its coiled conformation to prevent sidechain entanglement, leading to an extended backbone. As covalently linked constructs, they possess enhanced structural stability *in vivo* that enables their use as unimolecular carriers or as part of larger supramolecular assemblies. This enhanced stability in combination with their high molecular weight grants supramolecular assemblies formed from MPBs greater

stability compared to their linear counterparts.<sup>[14j]</sup> Furthermore, the bottom-up approach to synthesize MPBs (as with most polymeric NPs) renders them highly suitable for screening ideal NP physicochemical parameters for biomedical applications, since they can be fabricated to have single properties modified without changing others.<sup>[15]</sup>

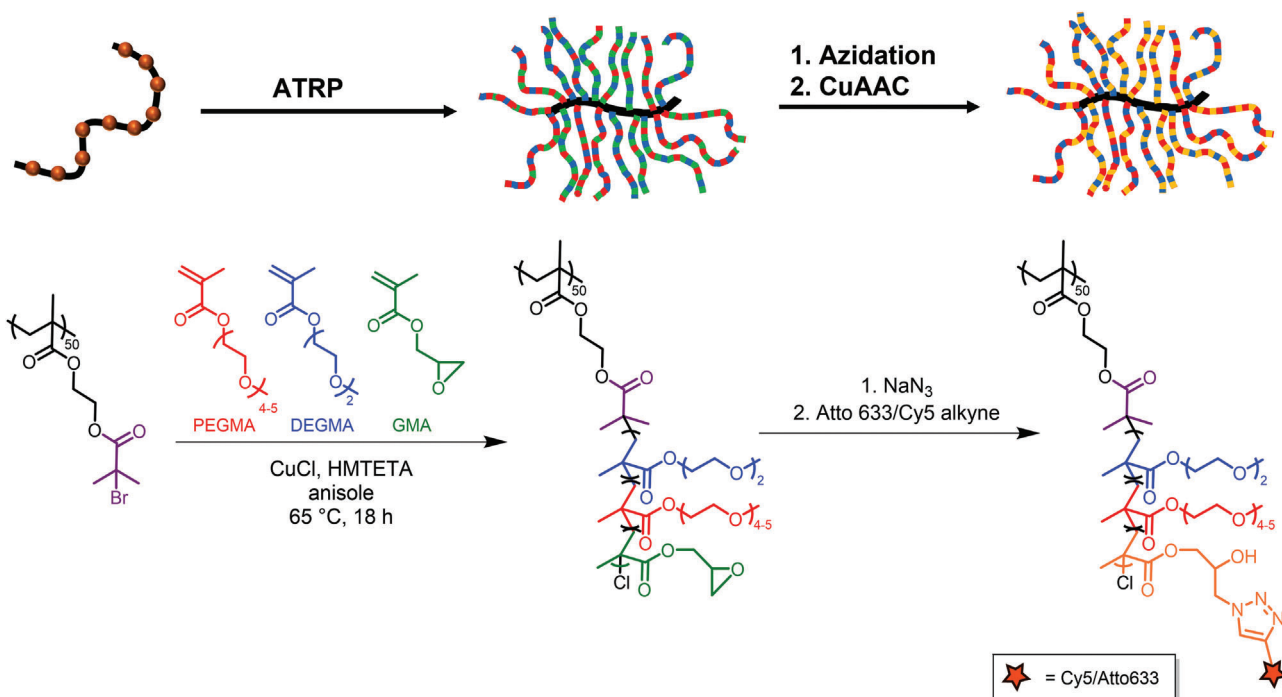
In this study, the potential influence of amphiphilicity was investigated in terms of NP accumulation and penetration into tumors and cancer cells, using MPBs as the NP platform. Briefly, a series of amphiphilic MPBs were produced from a poly(2-(2-bromoisobutyryloxy) ethyl methacrylate (PBIEM) backbone. Using reversible deactivation radical polymerization (RDRP) in a grafting from approach, the MPBs sidechains were then polymerized consisting of poly(ethylene glycol) methyl ether methacrylate (PEGMA,  $M_n = 300 \text{ g mol}^{-1}$ ), di(ethylene glycol) methyl ether methacrylate (DEGMA) and glycidyl methacrylate (GMA). Through systematically varying the feed ratio of the hydrophobic DEGMA and hydrophilic PEGMA monomers in the reaction feedstock, a series of amphiphilic MPBs were produced with similar sizes, surface charges and shapes, but variable hydrophobicity levels. Hence, the resultant polymeric NPs provided a reliable foundation to analyze the effect of increasing hydrophobicity independently of other parameters. These MPBs were subsequently incubated with 2D cancer cell monolayers along with more physiologically complex 3D multicellular tumor spheroids models to study their cellular uptake via confocal microscopy. Finally, the MPBs were further analyzed *in vivo* using a tumor xenograft model.

## 2. Results and Discussion

### 2.1. Synthesis and Characterization of Amphiphilic Molecular Polymer Bottlebrushes

In this study, four MPBs with different hydrophobicity levels were obtained from a common PBIEM backbone with a degree of polymerization (DP) of 50. After backbone preparation and post-modification, a “grafting-from” approach was employed via atom transfer radical polymerization (ATRP) to form random statistical sidechains composed of PEGMA, DEGMA and GMA (**Scheme 1**; Scheme S1, Supporting Information).

We were able to exert control over the amphiphilicity of each MPB by adjusting the PEGMA/DEGMA ratio in the reaction feedstock, which produced four well-defined and comparable MPBs bearing distinct the hydrophilic–hydrophobic balances. The MPBs are herein referred to as D0% (no DEGMA incorporated), D20% (20 mol% DEGMA), D40% (40 mol% DEGMA) and D60% (60 mol% DEGMA) (**Table 1**). Concurrently, a small fraction of GMA was copolymerized at a constant molar percentage of 5% to provide a handle for fluorophore labelling (Scheme 1). Sidechain and backbone monomer conversions were calculated via  $^1\text{H}$  NMR spectroscopy. Due to the bulky nature of the oligo(ethylene glycol) methacrylate, sidechain lengths were calculated using a 50% grafting efficiency. This grafting efficiency value has been experimentally reported for similar MPB systems using bulky monomers, such as PEGMA.<sup>[16]</sup> By only varying the molar ratio of PEGMA and DEGMA, and due to the similar reactivities of the methacrylate-based monomers, all MPBs of the series were obtained with similar sidechain DPs (Table 1).



**Scheme 1.** MPBs bearing different hydrophobicity levels are prepared using a combination of RDRP techniques. Control over the hydrophilic-hydrophobic balance in MPBs is granted by methodically varying the feedstock ratio of the hydrophilic PEGMA to the more hydrophobic DEGMA as part of the sidechain composition. Postpolymerization, the MPBs are functionalized with fluorophores (ATTO633 or Cy5) via a two-step process involving azidation of the GMA epoxide groups and then a copper-catalyzed azide-alkyne cycloaddition (CuAAC).

**Table 1.** Overview of characterization data of the synthesized MPBs.

| Sample name | Sidechain composition <sup>a)</sup>                                  | Sidechain DP <sup>a)</sup> | MW <sub>SEC</sub> <sup>b)</sup> [g mol <sup>-1</sup> ] | MW <sub>NMR</sub> <sup>a)</sup> [g mol <sup>-1</sup> ] | Hydrodyn. Diameter <sup>c)</sup> [nm] |
|-------------|--|----------------------------|--|--|---------------------------------------|
| D0%         | [PEGMA <sub>144</sub> -co-GMA <sub>8</sub> ]                         | 152                        | 358 000  | 1 110 000  | 40.0                                  |
| D20%        | [PEGMA <sub>120</sub> -co-DEGMA <sub>32</sub> -co-GMA <sub>8</sub> ] | 160                        | 318 000  | 1 079 000  | 46.1                                  |
| D40%        | [PEGMA <sub>88</sub> -co-DEGMA <sub>64</sub> -co-GMA <sub>8</sub> ]  | 160                        | 351 000  | 990 000  | 41.0                                  |
| D60%        | [PEGMA <sub>57</sub> -co-DEGMA <sub>98</sub> -co-GMA <sub>8</sub> ]  | 164                        | 346 000  | 923 000  | 40.0                                  |

<sup>a)</sup> Calculated by <sup>1</sup>H-NMR spectroscopy integrating double bond signals of monomers and considering a grafting efficiency of 50% from PBIEM backbones; <sup>b)</sup> Apparent average molecular weight  $M_n$  derived from DMAC SEC using monodisperse PMMA standards for calibration; <sup>c)</sup> Z-average derived DLS measurements of MPBs ( $c = 0.5 \text{ mg mL}^{-1}$ ) in PBS at 25 °C.

ensuring good comparability. The presence of GMA was also still detectable using NMR spectroscopy (Figure 1a). Size exclusion chromatography (SEC) was additionally used to determine the molecular weight distribution (MWD), as shown in Figure 1C). The SEC chromatograms confirmed the monomodal MWDs and high molecular weights of the four MPBs, albeit with the appearance of shoulders in the D40% and D60% chromatograms indicating minor intermolecular (brush-to-brush) coupling. All MPBs exhibited similar retention times in SEC, confirming their comparable hydrodynamic volumes. The apparent MW<sub>SEC</sub> was smaller than the calculated MW<sub>NMR</sub> because the chemical composition and architecture of the MPBs do not match the linear PMMA calibration standards. The MPB architecture also compacts the overall hydrodynamic volume leading to a shorter elution time (i.e., smaller MW) in SEC. Echoing the SEC findings, dynamic light scattering (DLS) analysis revealed that all MPBs possessed main populations with comparable hydro-

dynamic diameters ( $D_H$ ) in phosphate buffered saline (PBSx1) (Figure 1B). Measured Z-average  $D_H$  values included 40 nm (D0%), 46 nm (D20%), 41 nm (D40%), and 40 nm (D60%), and the smooth correlation functions for the samples supports the near-spherical morphologies adopted by the MPBs in solution (Figure S2, Supporting Information). The obtained DLS size distributions for D20%, D40%, and D60% indicate the presence of few larger aggregates. It should be noted that larger particle scatter disproportionately more and hence their appearance in the intensity-weighted plot is negligible. Finally, the Zeta potentials of the set of amphiphilic brushes was comparable around  $-0.02$  to  $0.04 \text{ mV}$ , which attested charge neutral surface properties.

Next, to gain insights into the varied hydrophilic-hydrophobic balances of our MPBs, we used DLS to determine the cloud point temperature ( $T_{CP}$ ) of each MPB by incrementally increasing the temperature of the solution to measure the resultant change in  $D_H$  (Figure 2).  $D_H$  was previously shown to be a suitable

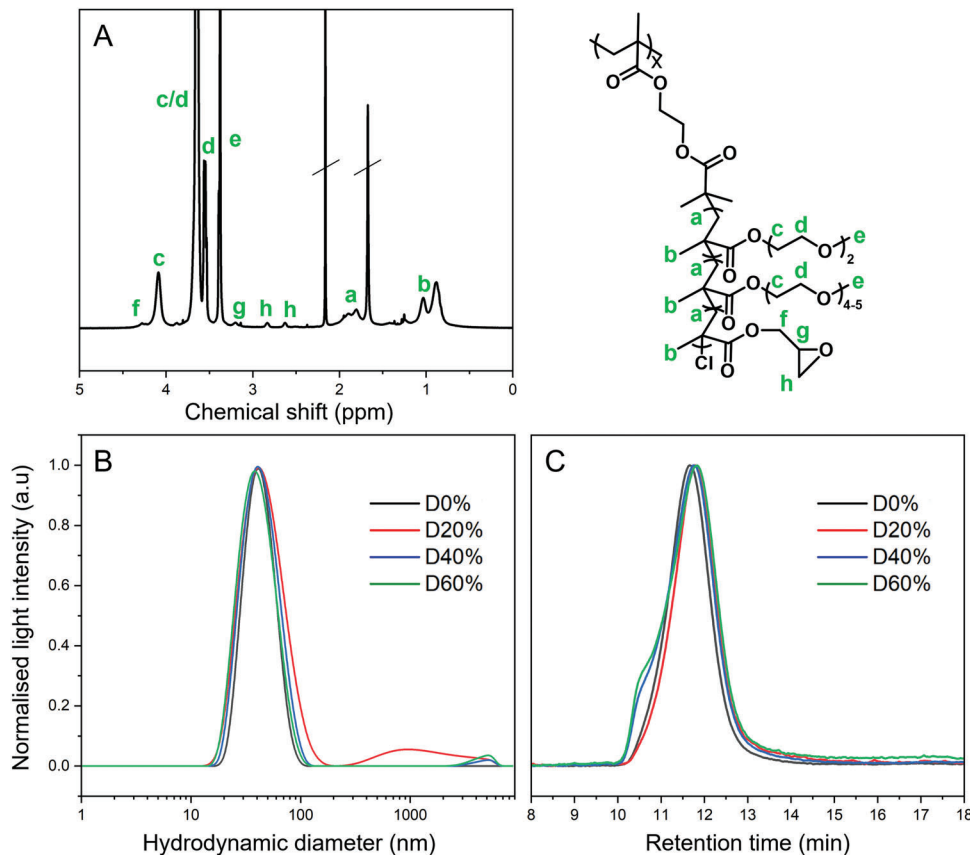


**Figure 1.** A) <sup>1</sup>H-NMR spectrum of D20% in CDCl<sub>3</sub> taken as a representative spectrum of all MPBs. B) Light intensity-weighted hydrodynamic size distributions of the four MPBs and C) SEC chromatograms obtained in DMAc (50 °C and 1 mL min<sup>-1</sup>); D0% (black), D20% (red), D40% (blue), and D60% (green).

parameter to gauge a varying hydrophilic to hydrophobic monomer ratio, as more hydrophobic macromolecules experience dehydration and intermolecular aggregation at lower temperatures.<sup>[17]</sup> In our case, the temperature at which significant aggregation was observed was noted as the T<sub>CP</sub>. In line with expectations, the T<sub>CP</sub> across the MPB series decreased as the percentage of incorporated DEGMA increased; from 55 °C (D0%), 49 °C (D20%), 39 °C (D40%), to 35 °C (D60%). Additionally, using a complementary measurement, this trend was repeated when the temperature-dependent optical transmittance of the MPB solutions were monitored by UV-vis spectroscopy (Figure S3, Supporting Information).

## 2.2. In Vitro and In Vivo Evaluation of MPBs Association with Cancer cells and Tumors

To facilitate live imaging and monitoring of the MPBs during in vitro and in vivo experiments via confocal microscopy and live and ex vivo animal/tissue imaging, the MPBs were subsequently functionalized with an azido group via a ring-opening reaction of GMA. Analysis of the functionalized brushes with <sup>1</sup>H-NMR spectroscopy showed no discernible signals which formerly belonged to the GMA epoxide group (Figure S4-1, Supporting Information), which was taken to mean the GMA units had

been successfully converted. The introduction of azido groups was also verified by infrared spectroscopy wherein a new signal denoting an azide stretch was detected in the spectrum of the modified MPBs (Figure S4-2, Supporting Information: ≈2100 cm<sup>-1</sup>). A copper-catalysed azide-alkyne cycloaddition (CuAAC) reaction was then used to “click” an ATTO 633- or Cy5-alkyne fluorophore to the MPBs.<sup>[14d,h]</sup> The extent of fluorophore labelling was in agreement with our targeted click ratio (≈1 dye molecule per MPB to not alter MPB surface properties) and confirmed qualitatively and quantitatively via UV-vis spectroscopy (Figure S5, Supporting Information).

After establishing the comparability of the MPBs in terms of size and shape, the effect of NP hydrophilic-hydrophobic balance on cancer cell interaction and uptake was investigated in vitro using confocal laser scanning microscopy (CLSM). First, DLD-1 cell monolayers were cultured with the MPBs ( $c = 0.2 \text{ mg mL}^{-1}$ ) at 37 °C for 24 h, then washed and imaged with CLSM (Figure 3). We observed significant association of MPBs with the cancer cells in the case of D0%, D20% and D40% judging from the high fluorescence intensity exhibited by these samples. Quantifying the red fluorescence using ImageJ, and by normalizing to D0%, the fluorescence associated with the cells increased 1.24-fold for D20% and 1.77-fold for D40% (Figure S6, Supporting Information). This suggested that with progressively increasing DEGMA content (ie. hydrophobicity levels), the MPBs increased their

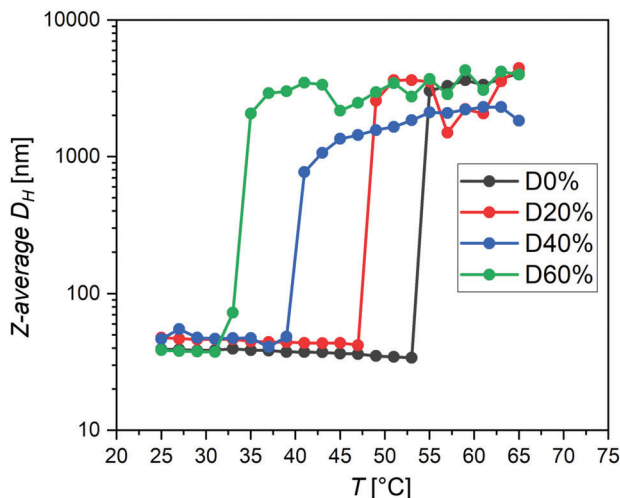


**Figure 2.** Indirect measurement of MPB hydrophilic-hydrophobic balance using cloud point temperatures obtained from DLS heating curves and the effect of temperature on the Z-average  $D_H$  for D0% (black), D20% (red), D40% (blue), and D60% (green). Measurements were taken using 0.5 mg mL<sup>-1</sup> MPB samples made in PBS.

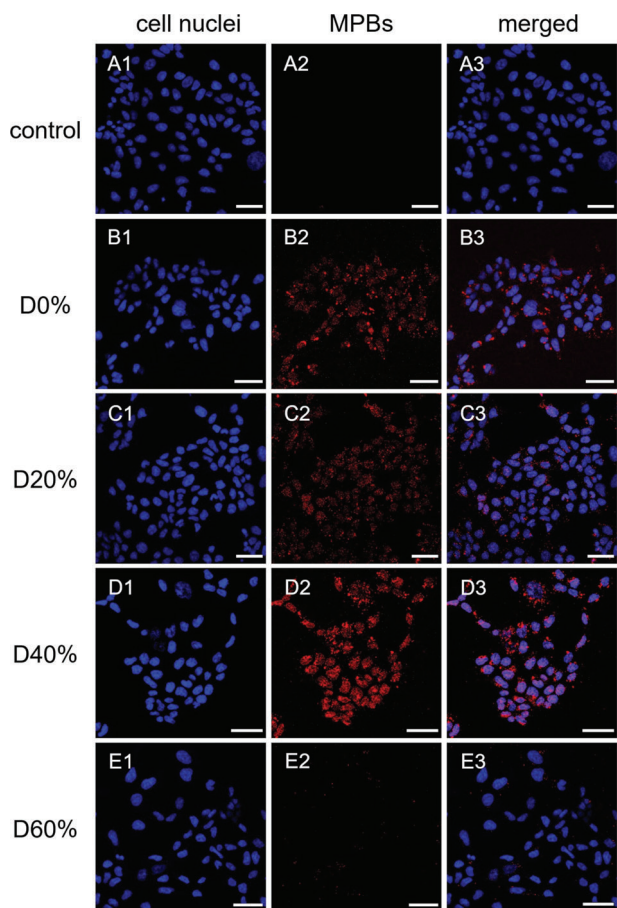


**Figure 3.** CLSM images of DLD-1 cancer cell monolayers after 24 h incubation with A) no MPBs (negative control), B) D0%, C) D20%, D) D40%, and E) D60%. Fluorescence channels are divided into series consisting of fluorescence emitted by A1–E1) cell nuclei, A2–E2) ATTO633-tagged MPBs and A3–E3) both nuclei and MPBs merged. Scale bars = 50  $\mu$ m.

association with the cells. However, D60% fluorescence was only half as much as D0% (0.51-fold decrease), indicating reduced association upon a certain degree of hydrophobicity.

Judging from the CLSM images (Figure 4), D60% showed no widespread cell association, but only a few very bright spots. The most likely explanation can be linked to the thermoresponsive behavior of the MPBs. At 37 °C, we anticipate that D60% would have completely collapsed and formed larger intermolecular aggregates, given its measured  $T_{CP}$  value is 35 °C. Thus, it is likely that the sufficiently large MPB aggregates (in excess of 5000 nm, see Figure 2) would prove too cumbersome to be sufficiently internalized by the cells, leading to low uptake and association. Therefore, D60% should be considered as an extreme case in which the  $T_{CP}$  is just below the temperature of incubation. On the other hand, in the case of D40%, the  $T_{CP}$  is also close to the incubation temperature (39 °C vs 37 °C respectively), but the MPB in this case is not (fully) collapsed and therefore did not aggregate in solution. There may however already be a possible onset of partial dehydration and collapse of its sidechains at a temperature that close to the  $T_{CP}$ . DLS of the brushes in complete media (e.g., in the presence of fetal bovine serum, FBS) did not reveal any unexpected protein-induced aggregation at 37 °C (Figure S7, Supporting Information).

The noticeable trend in the association assay with DLD-1 cells may be further explained by several theories that propose to explain this behavior. These theories have their basis in the important phase transition that certain polymers experience upon dehydration at higher temperatures, wherein the hydrogen bonds responsible for solubilizing the polymers in water are disrupted, causing inter- and intra-molecular hydrogen bonding to overcome and the polymer chains to collapse. The enhanced surface hydrophobicity has been posited to influence subsequent cell interactions via a few mechanisms, one of which is the increased non-specific adsorption of certain serum proteins that might promote non-specific phagocytic uptake. In their study using functionalized gold NPs, Salmaso et al. detected a significant increase in NP uptake when NPs were incubated above their  $T_{CP}$ .<sup>[18]</sup> In a similar vein, Kurzhals et al. detected an inverse correlation between cellular internalization and the  $T_{CP}$  of their SPION particles when functionalized with copolymers of 2-isopropyloxazoline (IPOx) and 2-ethoxyoxazoline (EtOx).<sup>[19]</sup> Using studies with HeLa cells, lower LCST values led to increased cellular uptake. Contrary to Salmaso et al. however, the trend between LCST and cell internalization was correlated to decreased hydration and consequently the formation of large, colloidally stable aggregates that might facilitate cell uptake. This falls in line with the general trend that larger particles (within certain limits) are much easier internalized than their smaller counterparts. Nonetheless, the explanations put forward in the literature so far do not adequately reconcile our in vitro findings. Therefore, more investigations need to be taken into the specific character of the MPBs in serum, as their interactions with surrounding proteins and ions may partly dictate their cellular interactions.

In a transition from 2D cell monolayers, the in vitro experiments were repeated with multicellular tumor spheroids (MCTSs) (Figure 4). Spheroids have increasingly been used in preclinical evaluations of anticancer nanomedicines since they embody the physiological complexities of in vivo tumor tissue more accurately than simple 2D tumor cell monolayers. Much

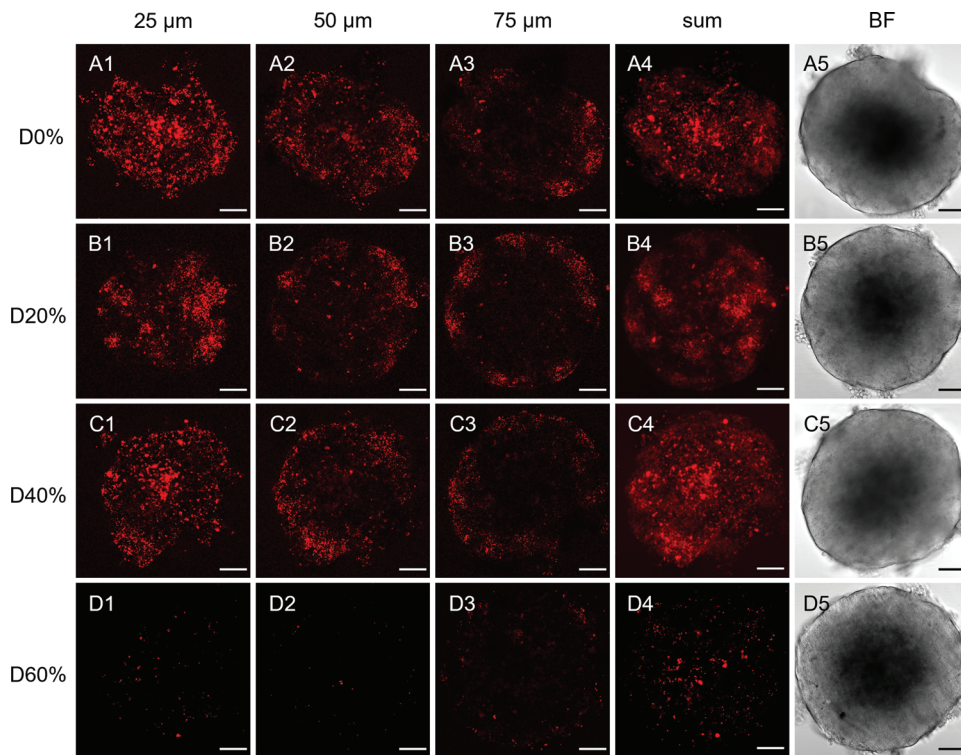


**Figure 4.** CLSM images of DLD-1 multicellular cancer cell spheroids after 24 h incubation showcasing different penetration levels of A) D0%, B) D20%, C) D40%, and D) D60% at different depths within the tumor (red fluorescence, columns 1–3). Sum images of z-stacks from 0 to 75  $\mu$ m were obtained to give an overall indication of A4–D4) each MPBs tumor penetration efficiency. A5–D5) Brightfield (BF) images of each tumor spheroid were also taken to establish spheroid viability. Scale bars = 100  $\mu$ m.

like tumors observed *in vivo*, sufficiently large MCTSs also exhibit layered cell populations due to heterogenous distribution of oxygen, nutrients and metabolic waste, with proliferative, healthy cells at the outer cell layers and necrotic cells residing in the tumor core.

To streamline analysis of MPB penetration into the MCTS, fluorescence images were captured at three equidistant depths (25, 50, and 75  $\mu$ m; Figure 4, A1/2/3-D1/2/3). The optical resolution of the microscope compromised image resolution beyond 150  $\mu$ m above the objective. However, there are noticeable differences in the apparent phantom tumor tissue penetration between the four MPBs. Most of the MPBs apart from D60% showed appreciable association at depths up to 50  $\mu$ m. From the observed fluorescence intensity, the extent of penetration for D0%, D20%, and D40% is not limited to the periphery of the tumor but the inner regions as well. However, at 75  $\mu$ m the three MPBs seem to be hindered from associating deeper towards the core. In contrast, D60% showed negligible association even at 25  $\mu$ m, a trend that we believe is due to similar reasons for the limited D60% uptake observed in the 2D monolayers (*i.e.*, formation of large aggregates unfavorable to tissue translocation and cellular internalization). Considering the sum of all red fluorescence across each sample, and by normalizing to D60%, the three MPBs that are not affected by the  $T_{CP}$  at the incubation temperature showed higher association, D0% (3.4-fold), D20% (2.1-fold), and D40% (4.5-fold) (Supporting Information S6, Supporting Information). To what extend the hydrophilic–hydrophobic balance affects spheroid penetration is subject of further investigation.

Next, we assessed the properties of the MPBs *in vivo* to better understand how the MPBs' hydrophilic–hydrophobic balance would impact their biodistribution and tumor homing properties. PEG-based MPBs had previously shown to exhibit long-circulating behavior *in vivo*.<sup>[14d,m,k]</sup> For these studies, azido-modified MPBs were fluorescently labelled with Cy5 (Figure S5-1, Supporting Information) to enable *in vivo* tracking using the IVIS imaging system. For the tumor xenograft model, we used nude mice with subcutaneous A2780 ovarian cancer cells; tumors were allowed to reach 200–300 mm<sup>3</sup> ( $\approx$ 11 days post-tumor challenge). Then Cy5-labeled MPBs were administered intravenously (500  $\mu$ g MPBs in 125  $\mu$ L PBS), and tumor-bearing mice were imaged at 9 h, 24 h, and 48 h post-MPB administration to monitor circulation and tissue deposition. Mice receiving the D0% MPB formulation showed minimal Cy5 fluorescence at any time point studies. In contrast, mice receiving the D20% and D40% MPB formulations showed increased Cy5 fluorescence at 9–48 h post-treatment. Diffuse fluorescence signals are observed which indicates that the MPBs remain in circulation with minimal organ clearance. The D60% formulation had distinct biodistribution with predominant Cy5 fluorescence accumulated in the spleen (Figure 5A; Figure S8A, Supporting Information).

To further quantify biodistribution, organs and tumors were collected and imaged *ex vivo* at 24 h and 48 h post-MPBs administration (Figure 5B,C; Figures S8B,C, S9, and S10, Supporting Information). Tissues were also homogenized, and a plate reader assay was used to quantify the Cy5 fluorescence in each tissue; by use of a standard curve (Figure S12A, Supporting Information),

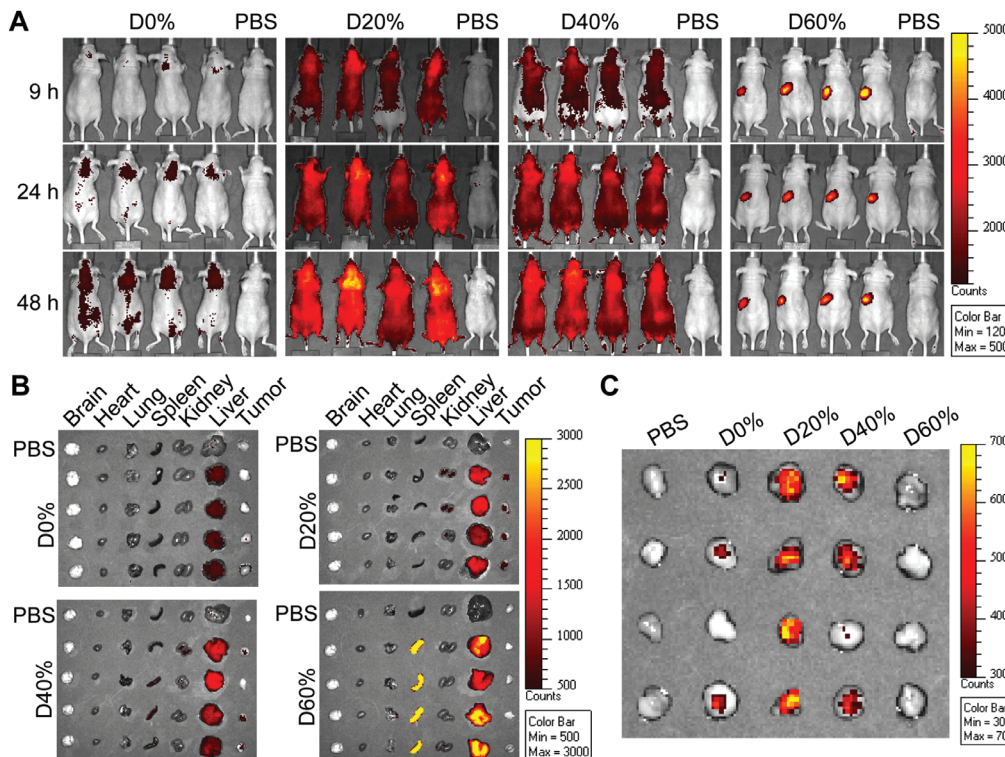


**Figure 5.** Biodistribution of Cy5-labeled MPBs postintravenous bolus administration using NCR nude mice with subcutaneous A2780 tumors; imaging was performed using an IVIS 200 system (Xenogen). a) Live animal imaging from dorsal at 9, 24, and 48 h. b) Major organs and tumors collected from mice at 48 h (organs at 24 h are shown in Figure S8 in the Supporting Information). c) Tumors from control and experimental groups at 48 h postinjections. (Tumors at 24 h postinjections are shown in Figure S9C in the Supporting Information).

the amount of MPBs per tissue was determined. Data indicate less tissue deposition of the D0% formulation versus any other formulation—future pharmacology studies are needed to detail the differences of the D0% formulation. D0%, D20%, and D40% showed the expected clearance through liver and spleen with accumulation slightly higher in the liver versus spleen (1.3 to 1.5 fold, Table 3); in stark contrast D60% showed exceptional high uptake in spleen versus liver (37 fold at 24 h, 23 fold at 48 h) (Figures 5B and **Figure 6A,D**; Figures S8C and S9B, Supporting Information; Table 3). Despite the dramatic difference for D60%, all MPBs were sequestered in spleen and liver (which are key components of the MPS system), indicating a dominantly macrophage-mediated clearance mechanism.<sup>[20]</sup> This tendency has been noticeably detected in our previous studies looking at biodistribution of MPBs with different aspect ratios and sizes.<sup>[14d,21]</sup> However, the uptake of D60% MPB by spleen at 48 h was extremely high with 1327 ng MPBs per mg spleen compared to D20% (21.2 ng mg<sup>-1</sup>) and D40% (31.7 ng mg<sup>-1</sup>) (Table 3). One explanation for this result could be that D60% having a heightened aggregation above its  $T_{CP}$  (35 °C), which is lower than the body temperature for mice at 36.6 °C, 40 whereas the other three MPB will remain stable with a size of ≈40 nm. NPs with size ranges of 10–200 nm are typically cleared by Kupffer cells in the liver and marginal zone (MZ) macrophages in the spleen.<sup>[22]</sup> As nanoparticle size increases, uptake may be increased in the spleen versus liver.<sup>[22]</sup> In particular, when NPs are larger than 200 nm they become too large to cross the endothelial slit of

**Table 2.** MPB accumulation levels in liver, spleen, and tumor at 24 and 48 h.

| MPB uptake [ng MPB mg <sup>-1</sup> organ] <sup>a)</sup> | D0%  |      | D20% |      | D40% |      | D60%   |        |
|--|------|------|------|------|------|------|--------|--------|
|  | 24 h | 48 h | 24 h | 48 h | 24 h | 48 h | 24 h   | 48 h   |
| Liver  | 16.2 | 21.1 | 21.2 | 29.9 | 30.7 | 45.5 | 27.3   | 57.3   |
| Spleen   | 13.0 | 14.6 | 14.5 | 19.6 | 20.9 | 31.7 | 1022.8 | 1327.0 |
| Tumor  | 5.2  | 3.2  | 6.3  | 8.5  | 6.2  | 8.0  | 2.0    | 2.3    |

<sup>a)</sup> Quantified based on Cy5 fluorescence intensity.

splenic sinuses and instead are filtered and retained in the red pulp of the spleen where the materials are eventually cleared by red-pulp resident macrophages.<sup>[23]</sup> Therefore, we attribute the splenic clearance and deposition of the D60% formulation as a result of aggregation.

Next, we analyzed tumor homing. IVIS imaging of tumors at 24 and 48 h showed Cy5 fluorescence for mice injected with D0%, D20%, and D40% MPBs (Figure 5C; Figure S9C, Supporting Information); this was further correlated to quantitative biodistribution analysis using the plate reader assay (Figure S12, Supporting Information). At 48 h, D20% and D40% MPBs were accumulated 2–3 fold higher than D0% MPBs as the mass of MPBs (in ng) per mass of tumor (in mg) (Figure 6B,E; **Table 2**). There was no apparent tumor homing for the D60% formulation

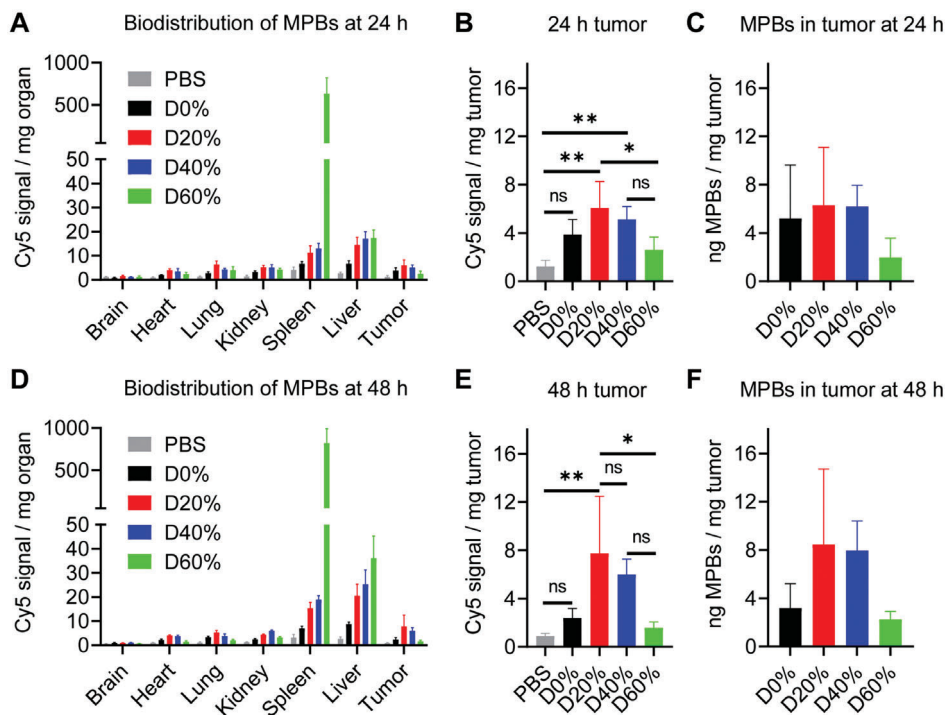


**Figure 6.** Biodistribution of Cy5-labeled MPBs postintravenous bolus administration in A2780 tumor-bearing NCR nude mice. Fluorescence signals of tissues at A,B) 24 h and D, E) 48 h postadministration were quantified by fluorescence plate reader measurement after tissue homogenization; the amount of MPBs accumulated in tumors at C) 24 h and F) 48 h was calculated based on a standard curve using known amounts of MPBs. Data are means  $\pm$  SEM ( $n = 4$ ), four mice each group. Statistical analysis was performed using ordinary one-way ANOVA and Turkey's multiple comparison test with \*  $p < 0.05$ , \*\*  $p < 0.01$ .

(see also discussion above). The general result is in accordance with the relative absence of D0% in the liver and spleen as discussed previously and explains the very low levels of D60% in the tumors due to its quick clearance by spleen. Comparing the MPB accumulation at 24–48 h, both D20% and D40% showed increase accumulation from  $\approx 6$  to  $\approx 8$  ng  $\text{mg}^{-1}$ , whereas D0% showed decreased accumulation and D60% remained the same throughout the incubation period (Figure 6C,F, Table 2).

NPs can accumulate in tumors through passive targeting due to enhanced permeability and retention (EPR) effect,<sup>[24]</sup> and the physical properties of NPs, e.g. size, shape, surface properties, can affect the efficacy in tumor homing.<sup>[5–8]</sup> Tumor homing of the four MPB may also be correlated with the varying degree of hydrophobicity. From D0% to D60%, MPB have increased hydrophobicity due to their composition. While in vitro studies clearly indicate that D0% particles are taken up by cancer cells and in 2D and 3D culture (Figure 3); in vivo studies indicate low tissue deposition and low tumor homing. The in vitro and in vivo profiles of the more hydrophobic formulations, D20% and D40%, suggest that a certain degree of hydrophobicity may be beneficial for nanomedical formulations—the D20% and D40% remained stable in vivo with favorable tumor deposition. Even though the obtained results correspond well with our observations of the MPBs interactions with in vitro models, the in vivo trend of MPB hydrophobicity versus tumor accumulation suggests that while hydrophilicity favors initial tumor uptake of the MPBs, a partially hydrophobic character is required for longer-term retention within tumor tissue.

### 3. Conclusion

This study has exploited the modular nature of MPB synthesis to fashion NPs with differing hydrophilic-hydrophobic character, thereby demonstrating their suitability as platforms that are able to orthogonally screen the biological effects of their physicochemical properties. Preliminary investigations into the NPs interactions with cancer cells models *in vitro* suggest that uptake is favored to a certain extent by particle hydrophilicity, with further work currently underway to clarify the uptake mechanism. Compelled by these observations, the biodistribution and tumor accumulation behavior of the MPBs were then studied *in vivo* using mice models. Despite the dominant sequestration of the particles in the renal and MPS clearance organs, significant differences were seen as a function of hydrophobicity wherein D60% exceeded the other MPBs in MPS organ uptake. The influence of increasing hydrophobicity also extended to penetration and retention within the mice tumors. Here, the least hydrophobic D0% showed inconsistent accumulation in tumor over time, whereas the more hydrophobic D20% and D40% showed increasing tumor deposition from 24 h to 48 h. Considering these results, appropriate future NP designs need to be tailored to have an appropriate hydrophobic-hydrophilic balance, not only to optimize early penetration into tumor but to also maintain adequate levels over time. Overall, the evaluations conducted into NP amphiphilicity conducted in this work implicate the hydrophilic-hydrophobic balance as a potential handle for control over NP-biological interactions.

## 4. Experimental Section

**Materials:** Di(ethylene glycol) methyl ether methacrylate (DEGMA, 95%), poly(ethylene glycol) methyl ether methacrylate (PEGMA, 95%,  $M_n = 300 \text{ g mol}^{-1}$ ), glycidyl methacrylate (GMA, 95%), 2-hydroxyethyl methacrylate (HEMA, 95%), 4-cyano-4-(thiobenzoylthio)pentanoic acid (CTBPA, 98%)  $\alpha$ -bromoisobutyryl bromide ( $\alpha$ -BiBB, 98%), 1,1,4,7,10,10-hexamethyltriethylenetetramine (HMTETA, 97%), atto633 alkyne (in DMSO, 1 mg mL<sup>-1</sup>), Cy5 alkyne (95%, in DMSO, 1 mg mL<sup>-1</sup>) and phosphate buffered saline (PBS) tablets were purchased from Merck (Sigma Aldrich, Australia). 4,4'-azobis(4-cyanovaleric acid) ( $V_{501}$ , pure solid, Alfa Aesar), copper(I) chloride (CuCl, ACS grade, Merck), ammonium chloride (NH<sub>4</sub>Cl, pure solid, Merck), sodium azide (NaN<sub>3</sub>, pure solid, Ajax), copper(II) sulfate pentahydrate (CuSO<sub>4</sub>·5H<sub>2</sub>O, pure solid, Ajax), anisole ( $\geq 99\%$ , Merck), *N,N*'-dimethylformamide (DMF,  $\geq 99\%$ , Ajax) and ethanol ( $\geq 99\%$ , Merck) were obtained as stated and used as received. PEGMA, DEGMA, GMA and HEMA were passed through a short silica column to remove inhibitors. Copper(I) chloride was purified by washing with glacial acetic acid, diethyl ether and ethanol. Dulbecco's Modified Eagle's Medium (with and without phenol red), Dulbecco's phosphate buffered saline (DPBS, no calcium or magnesium) and antibiotic-antimycotic solution containing penicillin and streptomycin (100 x) were purchased from Sigma Aldrich and ThermoFisher Scientific. RPMI 1640 media with L-glutamine were purchased from Corning. Fetal bovine serum (FBS) was purchased from R&D Systems. Trypsin-EDTA solution (0.5%, no phenol red) were purchased from Life Technologies. DLD-1 cells were sourced from Prof. Elizabeth New's research group at the School of Chemistry, University of Sydney. A2780 ovarian tumor cells were purchased from ATCC. Female NCR nu/nu mice were purchased from In-House Breeding Colony of UCSD. High concentration Matrigel Membrane Matrix was purchased from Corning.

**<sup>1</sup>H-NMR Spectroscopy:** Analyses were carried out on a Bruker Avance 300 spectrometer set at 300 MHz and 300 K. Samples were prepared in either deuterated chloroform or methanol.

**Size Exclusion Chromatography (SEC):** SEC analyses were performed using a UFC Shimadzu Prominence SEC system equipped with Phenogel™ columns (5  $\mu\text{m}$ , 10<sup>4</sup> Å and 10<sup>5</sup> Å). Dimethylacetamide (DMAc) containing butylhydroxytoluene (BHT, 0.05% w/w) and LiBr (0.03% w/w) was used as the eluent at a flow rate of 1 mL min<sup>-1</sup> at 50 °C. SEC samples were prepared by dissolution in DMAc and were passed through a 0.22  $\mu\text{m}$  syringe filter (nylon) before injection. Apparent molecular weights were derived from calibration with near monodisperse poly(methyl methacrylate) (PMMA) samples.

**Fluorescence Spectroscopy:** Measurements were performed using an Agilent Technologies Cary Eclipse Fluorescence Spectrophotometer. An excitation and emission slit size of 5 nm was used with an excitation wavelength of 630 and 650 nm for Atto633-labelled and Cy5-labelled MPB solutions respectively. Samples were analyzed at a concentration of 0.2 mg mL<sup>-1</sup> in a quartz microcuvette.

**Infrared Spectroscopy:** Measurements were carried out on a Perkin Elmer Spectrum Two FTIR spectrometer using samples dried from acetone.

**Dynamic Light Scattering (DLS):** DLS analysis was performed on a Malvern Zetasizer Nano ZS equipped with a He-Ne 633 nm laser. DLS was used to measure the hydrodynamic diameters and cloud point temperatures ( $T_{CP}$ ) of each MPB dispersed in PBSx1 (0.5 mg mL<sup>-1</sup>).  $T_{CP}$  measurements were obtained by measuring the Z-average hydrodynamic diameter at 2 °C increments from 25 to 67 °C with MPB solutions in PBSx1 (0.5 mg mL<sup>-1</sup>).

**Zeta Potential Measurements:** Measurements were carried out on a Malvern Zetasizer Nano ZS using MPB samples dispersed in PBS (2 mg mL<sup>-1</sup>).

**Synthesis of PHEMA:** HEMA (460 mg, 3.6 mmol), CTBPA (10 mg, 0.036 mmol) and  $V_{501}$  (2.5 mg, 9.0 mmol) were dissolved in DMF (1.5 mL) before undergoing three cycles of freeze-pump-thaw. The mixture was polymerized at 70 °C for 6 h before quenching via cooling and opening to air. The final product was purified by precipitating in diethyl ether and dissolving in DMF twice. Afterwards, the polymer was dissolved in a 2:1 mixture

**Table 3.** Reaction parameters for the four MPBs detailing the specific amounts of monomers used in the initial reaction feedstocks.

| MPB  | Reaction feedstock quantities |              |                |              |                |              |
|------|-------------------------------|--------------|----------------|--------------|----------------|--------------|
|      | PEGMA                         |              | DEGMA          |              | GMA            |              |
|      | mole<br>[mmol]                | mass<br>[mg] | mole<br>[mmol] | mass<br>[mg] | mole<br>[mmol] | mass<br>[mg] |
| D0%  | 3.34                          | 1001         | 0              | 0            | 0.18           | 25           |
| D20% | 2.63                          | 790          | 0.70           | 132          | 0.18           | 25           |
| D40% | 1.93                          | 580          | 1.40           | 264          | 0.18           | 25           |
| D60% | 1.23                          | 369          | 2.11           | 397          | 0.18           | 25           |

of dioxane and water before it was freeze-dried. Monomer conversion was calculated from <sup>1</sup>H-NMR spectroscopy based on the relative reduction of the vinyl proton signals ( $\approx 5.5$ –6.5 ppm) from the reaction mixture before and after polymerization.

**Synthesis of PBIEM:** PHEMA (170 mg, 1.26 mmol equiv. of hydroxyl groups) was dissolved in anhydrous pyridine (10 mL, dried over molecular sieves overnight) over ice.  $\alpha$ -BiBB (870 mg, 4.8 mmol) was added dropwise to the solution, after which the solution was stirred overnight at room temperature. For purification, the polymer was precipitated into MilliQ water, redissolved in THF and precipitated again into MilliQ water. The polymer was subsequently dissolved in dioxane for freeze-drying. See Section S1 in the Supporting Information for <sup>1</sup>H-NMR characterizations.

**Sidechain Grafting from PBIEM:** In a typical procedure used to make the four MPBs used in this study, PBIEM (5 mg, 0.018 mmol equiv. of Br), GMA (25 mg, 0.18 mmol) HMTETA (9.6  $\mu\text{L}$ , 0.018 mmol), and varying amounts of PEGMA and DEGMA were dissolved in anisole (5 mL). The mixture was degassed by three cycles of freeze-pump-thaw. Before the third freeze cycle, copper(I) chloride (1.8 mg, 0.018 mmol) was added to the mixture and the cycle was continued. The mixture was reacted at 65 °C for 18 h before quenching via cooling and exposure to air. Copper was removed by passing the mixture through a silica column. The product was partly purified by two cycles of precipitation and redissolving in cold hexane and anisole respectively. Lastly, the polymer brushes were dissolved in acetone and dialyzed (MWCO = 14 kDa) into acetone for storage. The DP of the sidechains was calculated from conversion as measured by <sup>1</sup>H-NMR, based on the relative reduction of the vinyl proton signals ( $\approx 5.5$ –6.5 ppm) in reaction feedstock samples before and after polymerization (taking into account a grafting efficiency of 50%). For the syntheses of the remaining MPBs, the protocol was followed with no changes except for the molar percentage of PEGMA and DEGMA fed into the reactions, (Table 3). The MPBs were denoted according to the molar percentage of the more hydrophobic DEGMA in their sidechains, ranging from the most hydrophilic D0% (no DEGMA, 95% PEGMA), D20% (20% DEGMA, 75% PEGMA, 5% GMA), D40% (40% DEGMA, 55% PEGMA, 5% GMA) and finally the most hydrophobic member D60% (60% DEGMA, 35% PEGMA, 5% GMA). The overall monomer conversions for each brush system were 38%, 40%, 40%, and 41%, respectively.

**Fluorophore Labelling of MPBs:** PBIEM-g-P(PEGMA-co-DEGMA-co-GMA) (40 mg,  $1.4 \times 10^{-6}$  mmol equiv. of GMA), sodium azide (10 mg, 0.15 mmol) and ammonium chloride (10 mg, 0.15 mmol) were dissolved in DMF (3 mL) and stirred overnight at 50 °C. The MPBs were then dialyzed once into a 1:1 acetone and methanol mixture, before being dialyzed again into neat acetone (MWCO = 3 kDa). PBIEM-g-P(PEGMA-co-DEGMA-co-GMA<sub>azide</sub>) (35 mg,  $7.9 \times 10^{-6}$  mmol), ATTO633 alkyne/Cy5 alkyne (20  $\mu\text{L}$ , 1 mg mL<sup>-1</sup> in DMSO), ascorbic acid (10 mg, 0.057 mmol) and CuSO<sub>4</sub>·5H<sub>2</sub>O (10 mg, 0.04 mmol) was dissolved in a mixture of water (2 mL) and methanol (1 mL). The solution was stirred in darkness at room temperature overnight. The mixture was dialyzed twice into acetone, then once into Milli-Q water (MWCO = 4 kDa). The labeled MPBs were subsequently stored in darkness to avoid photo-bleaching.

**DLD-1 Monolayer and Multicellular Tumor Spheroids (MCTS) Culturing/Uptake Assay:** DLD-1 colon cancer cell lines were grown in complete Dulbecco's Modified Eagle Medium (DMEM) supplemented with 10% (v/v) fetal bovine serum (FBS), 1% (v/v) penicillin/streptomycin and 1% L-glutamine at 37 °C and 5% CO<sub>2</sub>. Cells were sub-cultured at regular 3-day intervals with trypsin-EDTA. DLD-1 monolayers were cultured by pipetting 5 × 10<sup>4</sup> cells each into 35 mm µ-dishes (purchased from DKSH Holding AG) and incubating at 37 °C and 5% CO<sub>2</sub> in complete DMEM supplemented with 2% (v/v) FBS for 144 h. Afterwards, old growth media was carefully aspirated, washed with DPBS and replaced with DMEM-FBS solutions containing the MPBs (c = 0.2 mg mL<sup>-1</sup>, 2 mL total) and left to incubate for another 24 h. The samples were prepared for microscopic analysis by carefully draining the MPB-containing growth media, washing the monolayers twice with PBSx1, and adding 2 mL of DMEM (10% (v/v) FBS, no phenol red). ATTO633 intensity measurements of cell monolayers are presented as means ± SEM (n = 3). Fluorescence intensity analysis was performed in ImageJ. DLD-1 MCTSs were formed by pipetting 10<sup>4</sup> cells each in Corning Costar Ultra-Low Attachment 96-well plate (n = 4 wells per sample) and incubating for 72 h. For the uptake assay, MCTSs had their old media removed and replaced with DMEM-FBS solutions containing the MPBs (c = 0.5 mg mL<sup>-1</sup>, 200 µL per well) and left to incubate for another 24 h. After dosing and incubation, the spheroids had their old media carefully removed and were washed with DPBS twice to remove any unbound MPBs. Each spheroid was then transferred to 35 mm µ-dishes containing DPBS (1 mL) for imaging.

**Cell Culture and Tumor Inoculation:** A2780 ovarian tumor cells (ATCC) were cultured in RPMI media (Corning) with 10% (v/v) fetal bovine serum (FBS) (R&D Systems) and 1% (v/v) penicillin-streptomycin (ThermoFisher Scientific) and maintained at 37 °C with 5% CO<sub>2</sub>. All mice studies were approved by the Institutional Animal Care and Use Committee (IACUC) of the University of California, San Diego (UCSD). 6–8 weeks old female NCR nu/nu mice were purchased from In-House Breeding Colony of UCSD. Only female mice were considered because ovarian tumors were chosen as a mouse model. All mice were placed on Teklad 10 protein rodent diet (Envigo) for at least 10 days prior to any imaging procedures to minimize autofluorescence. 2 × 10<sup>6</sup> A2780 cells were suspended in 100 µL of culture media and Matrigel (Corning) at a 1:1 ratio and subcutaneously injected into the right flank of each mouse for tumor inoculation. All tumors were established and monitored closely till 11 days postinoculation, when all tumors reached 200–300 mm<sup>3</sup> in volume using the formula

$$v = l \times \frac{w^2}{2} \quad (1)$$

**Biodistribution of Injected MPBs:** On day 11 post-tumor inoculation, when tumors reached 200–300 mm<sup>3</sup>, 500 µg Cy5-labelled MPBs (D0%, D20%, D40%, and D60%) in 125 µL PBS were intravenously injected with n = 4 mice per group and one PBS control group. Two studies were conducted: a 24 h study, where all mice were imaged at 9 and 24 h postadministration of the MPBs or PBS using an IVIS 200 system (Xenogen); then mice were sacrificed, and organs and tumors collected for further analysis.

A 48-h study was carried out, where mice were imaged at 9 h, 24 h, and 48 h postadministration of the MPBs or PBS; then mice were sacrificed, and organs and tumors collected for further analysis. Organs (brain, heart, lung, spleen, kidney, and liver) and tumors were collected and imaged using the same setting for whole animal imaging. All images were processed and analyzed using the Living Image v2.5 software (Xenogen), and Cy5 fluorescence intensity of each organ was quantified. As a secondary method for quantification of the fluorescence signals from the brushes, tissues were weighed and homogenized within 1 mL PBS using a Cole-Parmer LabGEN 125 homogenizer. Homogenized samples were centrifuged at 8000 g for 5 min, and the tissue supernatant were collected to measure the Cy5 fluorescence using a Tecan Infinite M200 plate reader (excitation: 633 nm; emission: 665 nm; gain: 150); this experiment was done with n = 2 samples from each experimental group. Amounts of MPBs per tissue were calculated based on a standard curve using brushes of known concentration (Figure S11, Supporting Information).

**Statistical Analysis:** Data are presented as means ± SEM (n = 4). One-way analysis of variance (ANOVA) with Tukey's multiple comparison tests were used compare different groups (\*p < 0.05, \*\*p < 0.01, \*\*\*p < 0.001, \*\*\*\*p < 0.0001). All statistical tests were performed using GraphPad Prism v8.0 (GraphPad Software).

**Ethical Statement:** All animal experiments were carried out in accordance with the guidelines of the Institutional Animal Care and Use Committee (IACUC) of the University of California San Diego (UCSD) and approved by the Animal Ethics Committee of UCSD. We used 6–8 weeks old female NCR nu/nu mice from In-House Breeding Colony of UCSD and all mice were housed at the UCSD Moores Cancer Center with unlimited food and water.

## Supporting Information

Supporting Information is available from the Wiley Online Library or from the author.

## Acknowledgements

P.R. and Z.Z. contributed equally to this work. P.R. acknowledges financial support through an Australian Government Research Training Program (RTP) Scholarship. M.M. acknowledges funding via the Australian Research Council Future Fellowship (FT200100185) scheme. N.F.S. and M.M. acknowledge funding through The University of Sydney—University of California San Diego Partnership Collaboration Awards (PCA). N.F.S. acknowledges the NIH National Cancer Institute; work was funded in part through grant R01CA202814. The authors thank Dr. Sourabh Shukla (UC San Diego) for helpful discussion.

After initial online publication, the University of California, San Diego affiliations for Z.Z. and N.F.S. were corrected on March 11, 2022.

Open access publishing facilitated by The University of Sydney, as part of the Wiley - The University of Sydney agreement via the Council of Australian University Librarians.

## Conflict of Interest

The authors declare no conflict of interest.

## Data Availability Statement

The data that support the findings of this study are available from the corresponding author upon reasonable request.

## Keywords

3D cell culture, biodistribution, cellular interactions, polymer bottle-brushes, polymer nanoparticles, tumor mouse model

Received: January 20, 2022

Revised: February 13, 2022

Published online: February 27, 2022

- [1] a) A. R. Gardouh, B. M. Barakat, M. K. E. Qushawy, A. Y. El-kazzaz, M. M. Sami, S. A. Zaitone, *Chem. Biol. Interact.* **2018**, 295, 52; b) T. Shen, X. Xu, L. Guo, H. Tang, T. Diao, Z. Gan, G. Zhang, Q. Yu, *Biomacromolecules* **2017**, 18, 217; c) H. Maeda, G. Y. Bharate, J. Daruwalla, *Eur. J. Pharm. Biopharm.* **2009**, 71, 409; d) K. Chen, H. Cai, H. Zhang, H. Zhu, Z. Gu, Q. Gong, K. Luo, *Acta Biomater.* **2019**, 84, 339; e) L. Sun, H. Wei, X. Zhang, C. Meng, G. Kang, W. Ma, L. Ma, B. Wang, C. Yu, *Polym. Chem.* **2020**, 11, 4469.

- [2] a) J. Shi, P. W. Kantoff, R. Wooster, O. C. Farokhzad, *Nat. Rev. Cancer* **2017**, *17*, 20; b) Z. Cheng, M. Li, R. Dey, Y. Chen, *J. Hematol. Oncol.* **2021**, *14*, 85.
- [3] a) C. R. Thoma, M. Zimmermann, I. Agarkova, J. M. Kelm, W. Krek, *Adv. Drug Delivery Rev.* **2014**, *69*, 29; b) R. K. Jain, T. Stylianopoulos, *Nat. Rev. Clin. Oncol.* **2010**, *7*, 653; c) Y. H. Bae, K. Park, *J. Controlled Release* **2011**, *153*, 198.
- [4] S. Wilhelm, A. J. Tavares, Q. Dai, S. Ohta, J. Audet, H. F. Dvorak, W. C. W. Chan, *Nat. Rev. Mater.* **2016**, *1*, 16014.
- [5] a) L. Tang, N. P. Gabrielson, F. M. Uckun, T. M. Fan, J. Cheng, *Mol. Pharmaceutics* **2013**, *10*, 883. b) H. Cabral, Y. Matsumoto, K. Mizuno, Q. Chen, M. Murakami, M. Kimura, Y. Terada, M. R. Kano, K. Miyazono, M. Uesaka, et al, *Nat. Nanotechnol.* **2011**, *6*, 815.
- [6] V. P. Chauhan, Z. Popović, O. Chen, J. Cui, D. Fukumura, M. G. Bawendi, R. K. Jain, *Angew. Chem., Int. Ed.* **2011**, *50*, 11417.
- [7] a) D. Han, H. Qi, K. Huang, X. Li, Q. Zhan, J. Zhao, X. Hou, X. Yang, C. Kang, X. Yuan, *J. Mater. Chem. B* **2018**, *6*, 3331; b) B. Kim, G. Han, B. J. Toley, C. Kim, V. M. Rotello, N. S. Forbes, *Nat. Nanotechnol.* **2010**, *5*, 465; c) L. Zhang, P. Hao, D. Yang, S. Feng, B. Peng, D. Appelhans, T. Zhang, X. Zan, *J. Mater. Chem. B* **2019**, *7*, 953; d) C. He, Y. Hu, L. Yin, C. Tang, C. Yin, *Biomaterials* **2010**, *31*, 3657.
- [8] D. A. Christian, S. Cai, O. B. Garbuzenko, T. Harada, A. L. Zajac, T. Minko, D. E. Discher, *Mol. Pharmaceutics* **2009**, *6*, 1343.
- [9] S. Lindman, I. Lynch, E. Thulin, H. Nilsson, K. A. Dawson, S. Linse, *Nano Lett.* **2007**, *7*, 914.
- [10] T. Bewersdorff, A. Gruber, M. Eravci, M. Dumbani, D. Klinger, A. Haase, *Int. J. Nanomed.* **2019**, *14*, 7861.
- [11] D. F. Moyano, M. Goldsmith, D. J. Solfield, D. Landesman-Milo, O. R. Miranda, D. Peer, V. M. Rotello, *J. Am. Chem. Soc.* **2012**, *134*, 3965.
- [12] Y. Li, X. Chen, N. Gu, *J. Phys. Chem. B* **2008**, *112*, 16647.
- [13] R. Gupta, B. Rai, *Nanoscale* **2018**, *10*, 4940.
- [14] a) M. L. Ohnsorg, P. C. Prendergast, L. L. Robinson, M. R. Bockman, F. S. Bates, T. M. Reineke, *ACS Macro Lett.* **2021**, *10*, 375; b) F. Vohidov, L. E. Milling, Q. Chen, W. Zhang, S. Bhagchandani, H. V. T. Nguyen, D. J. Irvine, J. A. Johnson, *Chem. Sci.* **2020**, *11*, 5974; c) J. A. Johnson, Y. Y. Lu, A. O. Burts, Y. Xia, A. C. Durrell, D. A. Tirrell, R. H. Grubbs, *Macromolecules* **2010**, *43*, 10326; d) M. Müllner, S. J. Dodds, T. H. Nguyen, D. Senyschyn, C. J. H. Porter, B. J. Boyd, F. Caruso, *ACS Nano* **2015**, *9*, 1294; e) J. Zou, Y. Yu, Y. Li, W. Ji, C. K. Chen, W. C. Law, P. N. Prasad, C. Cheng, *Biomater. Sci.* **2015**, *3*, 1078; f) M. Müllner, K. Yang, A. Kaur, E. J. New, *Polym. Chem.* **2018**, *9*, 3461; g) T. Pelras, H. T. T. Duong, B. J. Kim, B. S. Hawkett, M. Müllner, *Polymer* **2017**, *112*, 244; h) A. Niederberger, T. Pelras, L. S. Manni, P. A. FitzGerald, G. G. Warr, M. Müllner, *Macromol. Rapid Commun.* **2021**, *42*, 2100138; i) M. Müllner, A. H. E. Müller, *Polymer* **2016**, *98*, 389; j) M. Müllner, *Macromol. Chem. Phys.* **2016**, *217*, 2209; k) A. Lu, F. Jia, X. Tan, D. Wang, X. Cao, J. Zheng, K. Zhang, *J. Am. Chem. Soc.* **2016**, *138*, 9097; l) L. Liao, J. Lia, E. C. Dreaden, S. W. Morton, K. E. Shopowitz, P. T. Hammond, J. A. Johnson, *J. Am. Chem. Soc.* **2014**, *136*, 5896; m) M. A. Sowers, J. R. McCombs, Y. Wang, J. T. Paletta, S. W. Morton, E. C. Dreaden, M. D. Boska, M. F. Ottaviani, P. T. Hammond, A. Rajca, J. A. Johnson, *Nat. Commun.* **2014**, *5*, 5460.
- [15] T. Pelras, C. S. Mahon, M. Müllner, *Angew. Chem., Int. Ed.* **2018**, *57*, 6982.
- [16] Z. Zheng, M. Müllner, J. Ling, A. H. E. Müller, *ACS Nano* **2013**, *7*, 2284.
- [17] S. Yamamoto, J. Pietrasik, K. Matyjaszewski, *Macromolecules* **2007**, *40*, 9348.
- [18] S. Salmaso, P. Caliceti, V. Amendola, M. Meneghetti, J. P. Magnusson, G. Pasparakis, C. Alexander, *J. Mater. Chem.* **2009**, *19*, 1608.
- [19] S. Kurzhals, N. Gal, R. Zirbs, E. Reimhult, *Nanoscale* **2017**, *9*, 2793.
- [20] A. Albanese, P. S. Tang, W. C. W. Chan, *Annu. Rev. Biomed. Eng.* **2012**, *14*, 1.
- [21] M. Müllner, D. C. Mehta, C. J. Nowell, C. J. H. Porter, *Chem. Commun.* **2016**, *52*, 9121.
- [22] M. Cataldi, C. Vigliotti, T. Mosca, M. R. Cammarota, D. Capone, *Int. J. Mol. Sci.* **2017**, *18*, 1249.
- [23] a) S. M. Moghimi, H. Hedeman, I. S. Muir, L. Illum, S. S. Davis, *Biochim. Biophys. Acta, Gen. Subj.* **1993**, *1157*, 233; b) S. M. Moghimi, A. C. Hunter, T. L. Andresen, *Annu. Rev. Pharmacol. Toxicol.* **2012**, *52*, 481; c) M. J. Ernsting, M. Murakami, A. Roy, S. D. Li, *J. Controlled Release* **2013**, *172*, 782; d) M. Demoy, J. P. Andreux, C. Weingarten, B. Gouritin, V. Guilloux, P. Couvreur, *Life Sci.* **1999**, *64*, 1329.
- [24] A. K. Iyer, G. Khaled, J. Fang, H. Maeda, *Drug Discovery Today* **2006**, *11*, 812.